Towards the use of conservative thermodynamic variables in data assimilation: preliminary results using ground-based microwave radiometer measurements

Pascal Marquet[1], Pauline Martinet[1], Jean-François Mahfouf[1], Alina Lavinia Barbu[1], and
Benjamin Ménétrier[2]

[1]CNRM, Université de Toulouse, Météo-France, CNRS, Toulouse, France
[2]INP, IRIT, Université de Toulouse, Toulouse, France

Correspondence: Pascal Marquet (pascal.marquet@meteo.fr, pascalmarquet@yahoo.com) Pauline Martinet
(pauline.martinet@meteo.fr)

Abstract. This study aims at introducing two conservative thermodynamic variables (moist-air entropy potential temperature and total water content) into a one-dimensional variational data assimilation system (1D-Var) to demonstrate the benefit for future operational assimilation schemes. This system is assessed using microwave brightness temperatures from a ground-based radiometer installed during the field campaign SOFGO3D dedicated to fog forecast improvement.

5   An underlying objective is to ease the specification of background error covariance matrices that are currently highly dependent on weather conditions making difficult the optimal retrievals of cloud and thermodynamic properties during fog conditions. Background error covariance matrices for these new conservative variables have thus been computed by an ensemble approach based on the French convective scale model AROME, for both all-weather and fog conditions. A first result shows that the use of these matrices for the new variables reduces some dependencies to the meteorological conditions (diurnal cycle, presence or not of clouds) compared to usual variables (temperature, specific humidity).

Then, two 1D-Var experiments (classical vs. conservative variables) are evaluated over a full diurnal cycle characterized by a stratus-evolving radiative fog situation, using hourly brightness temperatures.

Results show, as expected, that analysed brightness temperatures by the 1D-Var are much closer to the observed ones than background values for both variable choices. This is especially the case for channels sensitive to water vapour and liquid water.

15   On the other hand, analysis increments in model space (water vapour, liquid water) show significant differences between the two sets of variables.

1 Introduction

Numerical Weather Prediction (NWP) models at convective scale need accurate initial conditions for skillful forecasts of high impact meteorological events taking place at small-scale such as convective storms, wind gusts or fog. Observing systems

20   sampling atmospheric phenomena at small-scale and high temporal frequency are thus necessary for that purpose (Gustafsson et al., 2018). Ground-based remote-sensing instruments (e.g. rain and cloud radars, radiometers, wind profilers) meet such

requirements and provide information on wind, temperature, and atmospheric water (vapour and hydrometeors). Moreover, data assimilation systems are evolving towards ensemble approaches where hydrometeors can be initialized together with usual control variables. This is the case for the Météo-France NWP limited area model AROME (Seity et al., 2011; Brousseau et al., 2016) where, on top of wind (U, V), temperature (T) and specific humidity q_v, several hydrometeor mass contents can be initialized (cloud liquid water q_l, cloud ice water q_i, rain q_r, snow q_s and graupel q_g) (Destouches et al., 2021). However, these variables are not conserved during adiabatic and reversible vertical motion.

The accuracy of the analysed state in variational scheme highly depends on the specification of the so-called background error covariance matrix. Background error variances and cross-correlations between variables are known to be dependent on weather conditions (Montmerle and Berre, 2010; Michel et al., 2011). This is particularly the case during fog conditions with much shorter vertical correlation length-scales at the lowest levels and large positive cross-correlations between temperature and specific humidity (Ménétrier and Montmerle, 2011). In this context, Martinet et al. (2020) have demonstrated that humidity retrievals could be significantly degraded if sub-optimal background error covariances are used during the minimization. New ensemble approaches allow a better approximation of background error covariance matrices but rely on the capability of the ensemble data assimilation to correctly represent model errors, which might not always be the case during fog conditions. This is why it would be of interest to examine, in a data assimilation context, the use of variables that are more suitable when water phase changes take place.

It is well-known that data assimilation systems used to be based on the assumptions of homogeneity and isotropy of background error correlations. To release these hypotheses, Desroziers and Lafore (1993) and Desroziers (1997) implemented a coordinate change inspired by the semi-geostrophic theory to test flow-dependent analyses with case studies from the Front-87 field campaign (Clough and Testud, 1988), where the local horizontal coordinates were transformed into the semi-geostrophic space during the assimilation process. Another kind of flow-dependent analyses were made by Cullen (2003) and Wlasak et al. (2006) who proposed a low-order Potential Vorticity (PV) inversion scheme to define a new set of control variables. Similarly, analyses on potential temperature θ were made by Shapiro and Hastings (1973) and Benjamin et al. (1991), and more recently by Benjamin et al. (2004) with moist virtual θ_v and moist equivalent θ_e potential temperatures.

The aim of the paper is to test a one-dimensional data assimilation method that would be less sensitive to the average vertical gradients of the (T, q_v, q_l, q_i) variables. To this end, two conservative variables will be proposed, generalizing previous uses of θ (as a proxy for the entropy of dry air) to moist-air variables suitable for data assimilation. The new conservative variables are the total water content $q_t = q_v + q_l + q_i$ and the moist-air entropy potential temperature θ_s defined in Marquet (2011), which generalize the two well-known conservative variables (q_t, θ_l) of Betts (1973).

The focus of the study will be on a fog situation from the SOFOG3D field campaign using a one-dimensional variational (1D-Var) system for the assimilation of observed microwave brightness temperatures sensitive to T, q_v and q_l from a ground-based radiometer. Short-range forecasts from the convective scale model AROME (Seity et al., 2011) will be used as background profiles, the fast radiative transfer model RTTOV-gb (De Angelis et al., 2016; Cimini et al., 2019) will allow to accurately simulate the brightness temperatures, and suitable background error covariance matrices will be derived from an ensemble technique.

Section 2 presents the methodology (conservative variables, 1D-Var, change of variables). Section 3 describes the experimental setting, the meteorological context, the observations and the different components of the 1D-Var system. The results are commented in Section 4. Finally, conclusions and perspectives are given in Section 5.

60   ## 2   The methods

This section presents the methodology chosen for this study. The definition of the moist-air entropy potential temperature θ_s is introduced, as well as the formalism of the 1D-Var assimilation system, before describing the "conservative variable" conversion operator.

2.1   The moist-air entropy potential temperature

65   The moist-air entropy potential temperature θ_s is defined in Marquet (2011) to provide the same link with the specific entropy of moist air (s) as in Bauer (1908), leading to:

$$s = c_{pd} \ln\left(\frac{\theta_s}{T_0}\right) + s_{d0}, \tag{1}$$

where $c_{pd} \approx 1004.7 \, \mathrm{J\,K^{-1}\,kg^{-1}}$ is the specific heat of dry air at constant pressure, $T_0 = 273.15 \, \mathrm{K}$ a standard temperature and $s_{d0}(T_0, p_0) \approx 6775 \, \mathrm{J\,K^{-1}\,kg^{-1}}$ the reference dry air entropy at T_0 and at the standard pressure $p_0 = 1000 \, \mathrm{hPa}$.

70   Only the first order approximation noted $(\theta_s)_1$ in Marquet (2011) will be considered in the following, with:

$$\theta_s \approx (\theta_s)_1 = \theta \, \exp\left(-\frac{L_{vap}\, q_l + L_{sub}\, q_i}{c_{pd}\, T}\right) \exp(\Lambda_r\, q_t), \tag{2}$$

where $\theta = T\,(p/p_0)^{\kappa}$ is the dry-air potential temperature, p the pressure, $\kappa \approx 0.2857$, $L_{vap}(T)$ and $L_{sub}(T)$ the latent heat of vaporization and sublimation.

The first term θ in the right-hand side of (2) leads to a first conservation law (invariance) during adiabatic compression
75   and expansion and with the joint variations of T and p to keep θ constant. The first exponential explains another form of conservation law: due to reversible and adiabatic phase changes for which $c_{pd}\, dT \approx c_p\, dT = L_{vap}\, dq_l + L_{sub}\, dq_i$, with c_p the moist-air value and with therefore joint variations of the numerator and denominator of this first exponential, leaving this exponential invariant. It should be mentioned that the product of θ by the first exponential forms the Betts (1973) conservative variable θ_l.

80   While the Betts variable was established with the assumption of a constant total water content q_t, the second exponential in (2) sheds new light on conservation cases where the entropy of moist air can remain constant despite changes in the total water q_t. This occurs in regions where water vapour turbulence transport takes place, via the evaporation process over oceans, or at the edges of clouds via entrainment and detrainment processes.

We consider here "open-system" thermodynamic processes, for which the second exponential takes into account the impact
85   on moist-air entropy when the changes in specific content of water vapour is balanced, numerically, by opposite changes of that of dry air, namely with $dq_d = - dq_t \neq 0$. In this case, as stated in Marquet (2011), the changes in moist-air entropy depend

on reference values (with subscript "r") according to $d[\,q_d\,(s_d)_r + q_t\,(s_v)_r\,]$, and thus with $(s_d)_r$ and $(s_v)_r$ being constant and with the relation $q_d = 1 - q_t$, it leads to $[\,(s_v)_r - (s_d)_r\,]\,dq_t$.

This explains the new term $\Lambda_r = [(s_v)_r - (s_d)_r]/c_{pd} \approx 5.869 \pm 0.003$, which depends on the absolute reference entropies for water vapour $(s_v)_r \approx 12671\,\mathrm{J\,K^{-1}\,kg^{-1}}$ and dry air $(s_d)_r \approx 6777\,\mathrm{J\,K^{-1}\,kg^{-1}}$. This also explains that these "open-system" thermodynamic effects can be taken into account to highlight regimes where the specific moist-air entropy (s), θ_s and $(\theta_s)_1$ can be constant in spite of variable values of q_t, which may decrease or increase on the vertical (see Marquet, 2011, for such examples).

Although it should be possible to use $(\theta_s)_1$ as a control variable for assimilation, it appeared desirable to define an additional approximation of this variable for a more "regular" and more "linear" formulation, insofar as tangent-linear and adjoint versions are needed for the 1D-Var system. Considering the approximation $\exp(x) \approx 1 + x$ for the two exponentials in (2), neglecting the second order terms in x^2, also neglecting the variations of $L_v(T)$ with temperature and assuming a no-ice hypothesis $(q_i = 0)$, the new variable writes:

$$(\theta_s)_a = \theta \left[1 + \Lambda_r\, q_t - \frac{L_{vap}(T_0)\, q_l}{c_{pd}\, T} \right], \tag{3}$$

$$(\theta_s)_a = \frac{1}{c_{pd}} \left(\frac{p_0}{p} \right)^{\kappa} \left[c_{pd}\,(1 + \Lambda_r\, q_t)\, T - L_{vap}(T_0)\, q_l \right], \tag{4}$$

where $L_{vap}(T_0) \approx 2501\,\mathrm{kJ\,kg^{-1}}$. This formulation corresponds to S_m/c_{pd}, where S_m is the Moist Static Energy defined in Marquet (2011, Eq. 73) and used in the ECMWF[1] NWP global model by Marquet and Bechtold (2020).

The new potential temperature $(\theta_s)_a$ remains close to $(\theta_s)_1$ (not shown) and keeps almost the same three conservative properties described for $(\theta_s)_1$. This new conservative variable $(\theta_s)_a$ will be used along with the total water content $q_t = q_v + q_l$ in the data assimilation experimental context described in the following sections.

2.2 The 1D-Var formalism.

The 1D-Var data assimilation system searches for an optimal state (the analysis) as an approximate solution of the problem minimizing a cost function $\mathcal{J}$ defined by:

$$\mathcal{J}(x) = \frac{1}{2}\,(x - x_b)^T\,\mathbf{B_x}^{-1}\,(x - x_b)$$
$$+ \frac{1}{2}\,[\,y - \mathcal{H}(x)\,]^T\,\mathbf{R}^{-1}\,[\,y - \mathcal{H}(x)\,]. \tag{5}$$

The symbol ^{T} represents the transpose of a matrix.

The first (background) term measures the distance in model space between a control vector x (in our study, T, q_v and q_l profiles) and a background vector x_b, weighted by the inverse of the background error covariance matrix $(\mathbf{B_x})$ associated with the vector x. The second (observation) term measures the distance in the observation space between the value simulated from the model variables $\mathcal{H}(x)$ (in our study, the radiative transfer model RTTOV-gb) and the observation vector y (in our study, a

---

[1] European Centre for Medium range Weather Forecasts

set of microwave brightness temperatures from a ground-based radiometer), weighted by the inverse of the observation error covariance matrix ($\mathbf{R}$). The solution is searched iteratively by performing several evaluations of $\mathcal{J}$ and its gradient:

$$\nabla_x \mathcal{J}(x) = \mathbf{B_x}^{-1}(x - x_b) - \mathbf{H}^T \mathbf{R}^{-1}[y - \mathcal{H}(x)],$$
(6)

where $\mathbf{H}$ is the Jacobian matrix of the observation operator representing the sensitivity of the observation operator to changes
120 in the control vector x.

2.3 The conversion operator

The 1D-Var assimilation defined previously with the variables $x = (T, q_v, q_l)$ can be modified to use the conservative variables $z = ((\theta_s)_a, q_t)$. A conversion operator that projects the state vector from one space to the other can be written as $x = \mathcal{L}(z)$. In the presence of liquid water q_l, an adjustment to saturation is made to separate its contribution to the total water content q_t from
125 the water vapour content q_v. This is equivalent to distinguishing the "unsaturated" case from the "saturated" one. Therefore, starting from initial conditions $(T_I, q_I) = (T, q_v)$ and using the conservation of $(\theta_s)_a$ given by Eq. (4), we look for the variable T^* such that:

$$T^* + \alpha\, q_{sat}(T^*) = T_I + \alpha\, q_I,$$
(7)

$$\text{where } \alpha = \frac{L_{vap}(T_0)}{c_{pd}\,(1 + \Lambda_r\, q_t)}$$
(8)

130 and $q_{sat}(T^*)$ is the specific humidity at saturation.

For the unsaturated case ($q_v < q_{sat}(T^*)$), we obtain the variables (T, q_v, q_l) directly from Eq. (4):

$$q_l = 0\,, \ \ q_v = q_t \ \text{ and } \ T = (\theta_s)_a \left(\frac{p}{p_0}\right)^\kappa \frac{1}{1 + \Lambda_r\, q_t}.$$
(9)

For the saturated case ($q_v \geq q_{sat}(T^*)$), we write:

$$q_l = q_t - q_{sat}(T^*) \ \text{ and } \ q_v = q_{sat}(T^*).$$
(10)

135 In this situation, it is necessary to calculate implicitly the temperature T^*, given by Equation (7). We compute numerically an approximation of T^* by an iterative Newton's algorithm.

Taking into account this change of variables, the cost-function can be written as:

$$\mathcal{J}(z) = \frac{1}{2}(z - z_b)^T \mathbf{B_z}^{-1}(z - z_b)$$
$$+ \frac{1}{2}[y - \mathcal{H}(\mathcal{L}(z))]^T \mathbf{R}^{-1}[y - \mathcal{H}(\mathcal{L}(z))].$$
(11)

140 Then, its gradient given by Eq. (6) becomes:

$$\nabla_z \mathcal{J}(z) = \mathbf{B_z}^{-1}(z - z_b) - \mathbf{L}^T \mathbf{H}^T \mathbf{R}^{-1}[y - \mathcal{H}(\mathcal{L}(z))],$$
(12)

where $\mathbf{L}^T$ is the adjoint of the conversion operator $\mathcal{L}$.

3 The experimental set-up

The numerical experiments to be presented afterwards will use measurements made during the SOFOG3D field experiment[2]

145 (SOuth west FOGs 3D experiment for processes study) that took place from 1 October 2019 to 31 March 2020 in southwestern France to advance understanding of small-scale processes and surface heterogeneities leading to fog formation and dissipation.

Many instruments were located at the Saint-Symphorien super-site (Les Landes region), such a HATPRO microwave radiometer (Rose et al., 2005), a 95 GHz BASTA Doppler cloud radar (Delanoë et al., 2016), a Doppler lidar, an aerosol lidar, a surface weather station and a radiosonde station. One objective of this campaign was to test the contribution of the assimilation

150 of such instrumentation on the forecast of fog events by NWP models.

3.1 The 9 February 2020 situation

This section presents the experimental context of 9 February 2020 at the Saint-Symphorien site characterized by (i) a radiative fog event observed in the morning and (ii) the development of low-level clouds in the afternoon and evening.
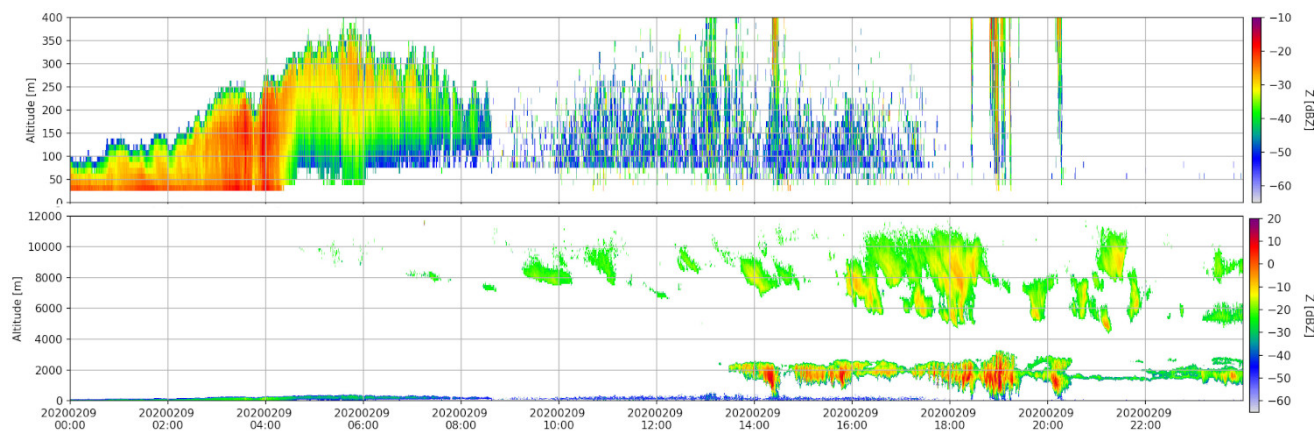
Figure 1. Reflectivity profiles at 95 GHz (dBZ) measured by the BASTA cloud radar in the first 500 m (top) and up to 12000 m altitude (bottom), with UTC hours in abscissas, for the day of 9 February 2020 at Saint-Symphorien (Les Landes region). From http://basta.projet. latmos.ipsl.fr/?bi=bif

Figure 1 shows a time series of cloud radar reflectivity profiles (W-band at 95 GHz) measured by the BASTA instrument

155 (Delanoë et al., 2016) in the first few hundred meters (top panel) between 9 February 2020 at 00 UTC and 10 February 2020 at 00 UTC. The instrument reveals a thickening of the fog between midnight and 04 UTC. The fog layer thickness is located between 90 m and 250 m. After 04 UTC, the fog layer near the ground rises, lifting in a "stratus" type cloud (between 100 and 300 m). After 08 UTC, the stratus cloud dissipates. In the bottom panel BASTA observations up to 12000 m ($\approx$ 200 hPa) indicate low-level clouds after 14 UTC, generally between 1000 m ($\approx$ 900 hPa) and 2000 m ($\approx$ 780 hPa), with a fairly good

[2]https://www.umr-cnrm.fr/spip.php?article1086

160   agreement with AROME short-range (1 h) forecasts (see Fig. 2 (f)). Optically thin (reflectivity below 0 dBZ) high altitude ice
clouds are also captured by the radar.
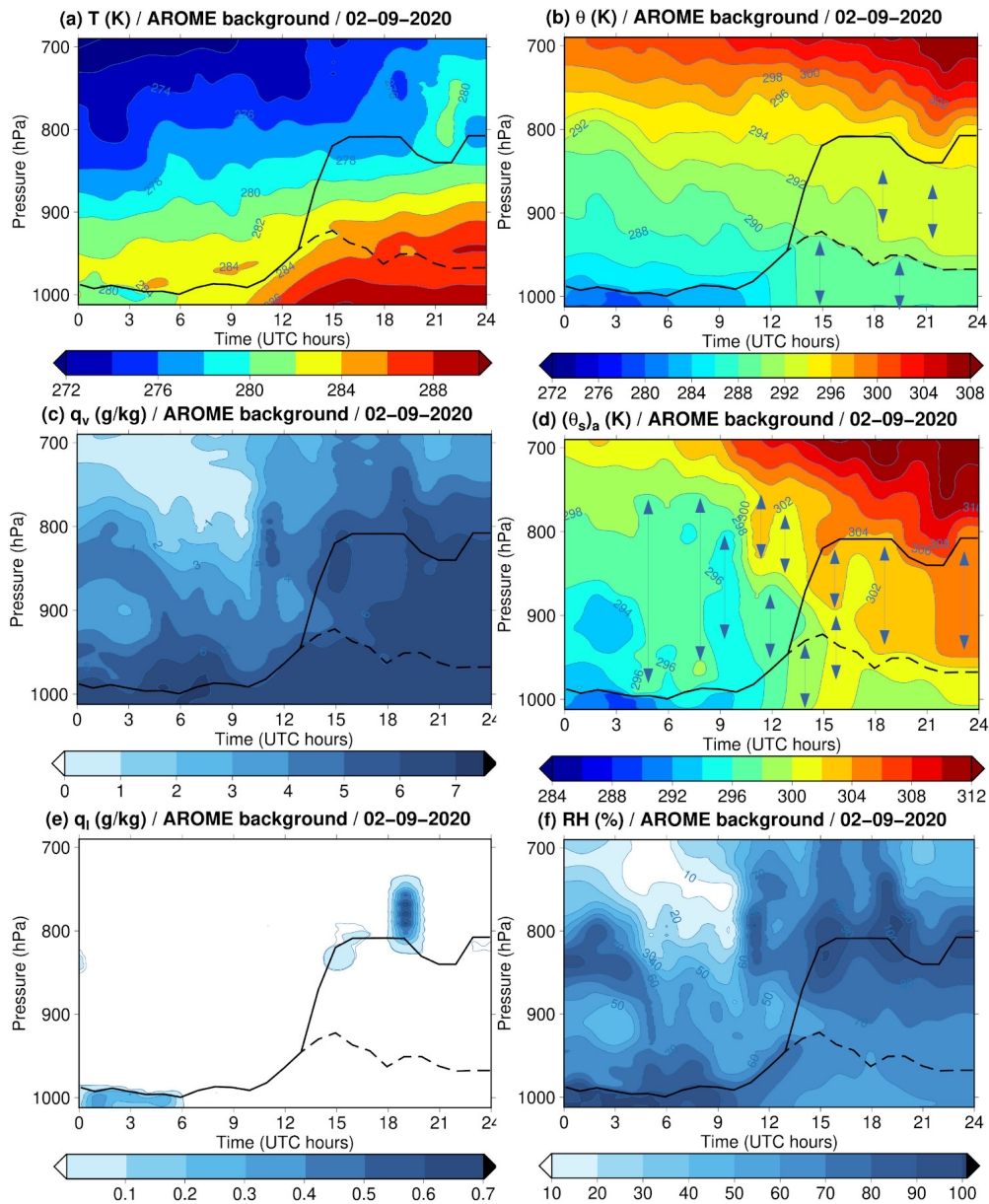
Figure 2. Vertical profiles derived from 1 h forecasts of AROME background for all hours of the day 9 February 2020 at Saint-Symphorien
(Les Landes region in France) for: (a) absolute temperature T every 0.2 K; (b) dry-air potential temperature θ every 0.2 K, (c) water-vapour
specific content q_v every 1 g/kg, (d) entropy potential temperature $(\theta_s)_a$ every 0.2 K, (e) cloud liquid-water specific content q_l (contoured
for 0.00001 g/kg and 0.002 g/kg, then every 0.1 g/kg above 0.1 g/kg) and (f) Relative Humidity (RH) every 10 %. The black curves (solid
and dashed lines) represent the PBL heights determined from maximum of vertical gradients of θ.

Figure 2 depicts the diurnal cycle evolution in terms of vertical profiles of: (a) absolute temperature T, (b) dry-air potential temperature θ, (c) water vapour specific content q_v, (d) entropy potential temperature $(\theta_s)_a$, (e) cloud liquid water specific content q_l and (f) relative humidity (RH), from 1 h AROME forecasts (background) of 9 February 2020 at Saint-Symphorien.

165   At this stage, it is important to indicate that the AROME model has a 90-level vertical discretisation from the surface up to 10 hPa, with a high resolution in the Planetary Boundary Layer (PBL) since 20 levels are below 2 km.

Figures 2 (e) and (f), for q_l and RH, show two main saturated layers: a fog layer close to the surface between 00 and 09 UTC with the presence of a thin liquid cloud layer aloft at 850 hPa at 00 UTC, and the presence of a stratocumulus cloud between 14 UTC and midnight at 850 hPa. During the night, near surface layers cool down, with a thermal inversion that sets at around 170   01 UTC and persists until 07 UTC. After the transition period between 06 UTC and 09 UTC, when the dissipation of the fog and stratus takes place, the air warms up and the PBL develops vertically (see the black curves plotted where vertical gradients of θ in (b) are large). Towards the end of the day, the thickness of the PBL remains important until 24 UTC, probably due to the presence of clouds between 800 and 750 hPa that reduces the radiative cooling (see Figs. 2 (c) and (f) for q_v and RH).

Figure 2(d) reveals weaker vertical gradients for the $(\theta_s)_a$ profiles, notably with contour lines often vertical and less numer-175   ous than those of the T, θ and q_v profiles in (a), (b) and (c), as also shown by more extensive and more numerous vertical arrows in (d) than in (b). Here we see the impact of the coefficient $\Lambda_r \approx 5.869$ in Eqs. (3)-(4), which allows the vertical gradients of θ in (b) and q_v in (c) to often compensate each other in the formula for $(\theta_s)_a$. This is especially true between 980 hPa and 750 hPa in the morning between 04 and 10 UTC, and also within the dry and moist boundary layers during the day.

Note that the dissipation of the fog is associated with a homogenization of $(\theta_s)_a$ in (d) from 04 to 05 UTC in the whole 180   layer above, in the same way as the transition from strato-cumulus toward cumulus was associated with a cancellation of the vertical gradient of $(\theta_s)_1$ in the Fig. 6 of Marquet and Geleyn (2015). This phenomenon cannot be easily deduced from the separate analysis of the gradients of θ and q_v in (b) and (c). Therefore, three air mass changes can be clearly distinguished during the day. The vertical gradients of $(\theta_s)_a$ are stronger during cloudy situations, first (i) at night and early morning before 04 UTC and just above the fog, then (ii) at the end of the day above the top-cloud level at 800 hPa; with (iii) turbulence-related 185   phenomena in between that mix the air mass and $(\theta_s)_a$, up to the cloudy layer tops that evolve between 950 and 800 hPa from 13 UTC to 17 UTC.

The observations to be assimilated are presented in the following. The HATPRO (Humidity And Temperature PROfiler) MicroWave Radiometer (MWR) measures brightness temperatures (TB) at 14 frequencies (Rose et al., 2005) between 22.24 and 58 GHz: 7 are located in the water vapour absorption band and 7 are located in the oxygen absorption band. For our 190   study, one of the channels (at 23.84 GHz) was eliminated because of a receiver failure identified during the campaign. In this preliminary study, we have only considered the zenith observation geometry of the radiometer for the sake of simplicity.

The radiative transfer model $\mathcal{H}$ needed to simulate the model equivalent of the observations, together with the choice of the control vector and the specification of the background and observation error matrices, are presented in the next section.

3.2 The components of the 1D-Var

195 In 1D-Var systems, the integrated liquid water content, Liquid Water Path (LWP) can be included in the control vector x as initially proposed by Deblonde and English (2003) and more recently used by Martinet et al. (2020). A first experimental set-up has been defined where the minimization is performed with the control vector being (T, q_v, LWP). It will be considered as the reference being named "REF". The 1D-Var system chosen for the present study is the one developed by the EUMETSAT NWP SAF[3], where the minimisation of the cost-function is solved using an iterative procedure proposed by Rodgers (1976)

200 with a Gauss-Newton descent algorithm.

During the minimization process, only the amount of integrated liquid water is changed. In this approach, the two "moist" variables q_v and LWP are considered to be independent (no cross-covariances for background errors between these variables). The second experimental framework, where the control vector is $z = ((\theta_s)_a, q_t)$, corresponding to the conservative variables, is named "EXP". The numerical aspects of the 1D-Var minimisation are kept the same as in "REF".

205 Then, a set of reference matrices $\mathbf{B_x}(T, q_v)$ has been estimated every hour using the Ensemble Data Assimilation (EDA) system of the AROME model on 9 February 2020. These matrices were obtained by computing statistics from a set of 25 members providing 3 h forecasts for a subset of 5000 points randomly selected in the AROME domain to obtain a sufficiently large statistical sample. Then, matrices associated with fog areas, and noted $\mathbf{B_x}(T, q_v)_{fog}$, were computed every hour by applying a fog mask (defined by areas where q_l is above $10^{-6}\ kg\,kg^{-1}$ for the three lowest model levels), in order to select

210 only model grid points for which fog is forecast in the majority of the 25 AROME members. The background error covariance matrices $\mathbf{B_z}((\theta_s)_a, q_t)$ and $\mathbf{B_z}((\theta_s)_a, q_t)_{fog}$ were obtained in a similar way.

The observation errors are those proposed by Martinet et al. (2020) with values between 1 and 1.7 K for humidity channels (frequencies between 22 and 31 GHz), values between 1 and 3 K for transparent channels affected by larger uncertainties in the modelling of the oxygen absorption band (frequencies between 51 and 54 GHz) and values below 0.5 K for the most opaque

215 channels (frequencies between 55 and 58 GHz).

The RTTOV[4] radiative transfer model is used to calculate brightness temperatures in different frequency bands from atmospheric temperature, water vapour and hydrometeor profiles together with surface properties (provided by outputs from the AROME model). This radiative transfer model has been adapted to simulate ground-based microwave radiometer observations (RTTOV-gb) by De Angelis et al. (2016).

4 Numerical results

220

The 1D-Var algorithm was tested on the day of 9 February 2020 with observations from the HATPRO microwave radiometer installed at Saint-Symphorien. This section presents and discusses the results obtained on three aspects: (1) the study of background error cross-correlations; (2) the performance of the 1D-Var assimilation system in observation space by examining the

---

[3]Numerical Weather Prediction Satellite Application Facility
[4]Radiative Transfer for the TIROS Operational Vertical Sounder

fit of simulated TB with respect to the observed ones; and (3) in model space in terms of analysis increments for temperature,
specific humidity and liquid water content.

4.1 The background error cross correlations

Figure 3 displays for the selected day at 06 UTC the cross-correlations between T and q_v (top) and between $(\theta_s)_a$ and q_t
(bottom), with (right) and without (left) fog mask. For the classical variables the correlations are strongly positive in the
saturated boundary layer with the fog mask from levels 75 to 90 (between 1015 and 950 hPa), while with profiles in all-
weather conditions the correlations between T and q_v are very weak in the lowest layers. On the other hand, the atmospheric
layers above the fog layer exhibit negative correlations between temperature and specific humidity along the first diagonal.

When considering conservative variables, the correlations along the diagonal show a consistently positive signal in the
troposphere (below level 20 located around 280 hPa). Contrary to the classical variables, which are rather independent in clear-
sky atmospheres as previously shown by Ménétrier and Montmerle (2011), the $\mathbf{B_z}$ matrix reflects the physical link between
the two new variables as diagnosed from the AROME model. The correlations are positive with and without fog mask. This
result shows that the matrix $\mathbf{B_z}(\theta_s, q_t)$ is less sensitive to fog conditions than the $\mathbf{B_x}$ matrix. It could therefore be possible
to compute a $\mathbf{B_z}(\theta_s, q_t)$ matrix without any profile selection criteria that would be nevertheless suitable for fog situations,
resulting in a more robust estimate. This result is key for 1D-Var retrievals which are commonly used in the community of
ground-based remote sensing instruments to provide databases of vertical profiles for the scientific community. In fact, the
accuracy of 1D-Var retrievals is expected to be more robust with less flow-dependent $\mathbf{B}$ matrices.

It has also been noticed that these background error statistics are less dependent on the diurnal cycle and on the meteorolog-
ical situation (e.g. in the presence of fog at 06 UTC and low clouds at 21 UTC), contrary to the $\mathbf{B_x}(T, q_v)$ matrix where there
is a reduction in the area of positive correlation in the lowest layers between 06 UTC and 21 UTC (Fig. 4).

The 1D-Var results are now assessed in observation space by examining innovations (differences between observed and
simulated brightness temperatures) from AROME background profiles and residuals. In the following, we have only used
background error covariance matrices estimated at 06 UTC with fog mask, for a simplified comparison framework of the two
1D-Var systems.

4.2 1D-Var analysis fit to observations

Figure 5 presents both (a) innovations and (b,c) residuals obtained with the two 1D-Var systems (b: REF and c: EXP) for the
13 channels and for each hour of the day. The innovations are generally positive for water vapour sensitive channels during the
day, and negative for temperature channels, especially in the morning. The differences are mostly between -2.5 and 5 K. For
channels 6, 7 and 8, which are sensitive to liquid water content, the innovations can reach higher values exceeding 10 K (in the
afternoon) or being around -5 K (in the morning).

In terms of residuals, as expected from 1D-Var systems, both experiments significantly reduce the deviations of the observed
TB from those calculated using the background profiles, especially for the first eight channels sensitive to water vapour
and liquid water. The temperature channels used in the zenith mode are modified less or very little, the deviations from the
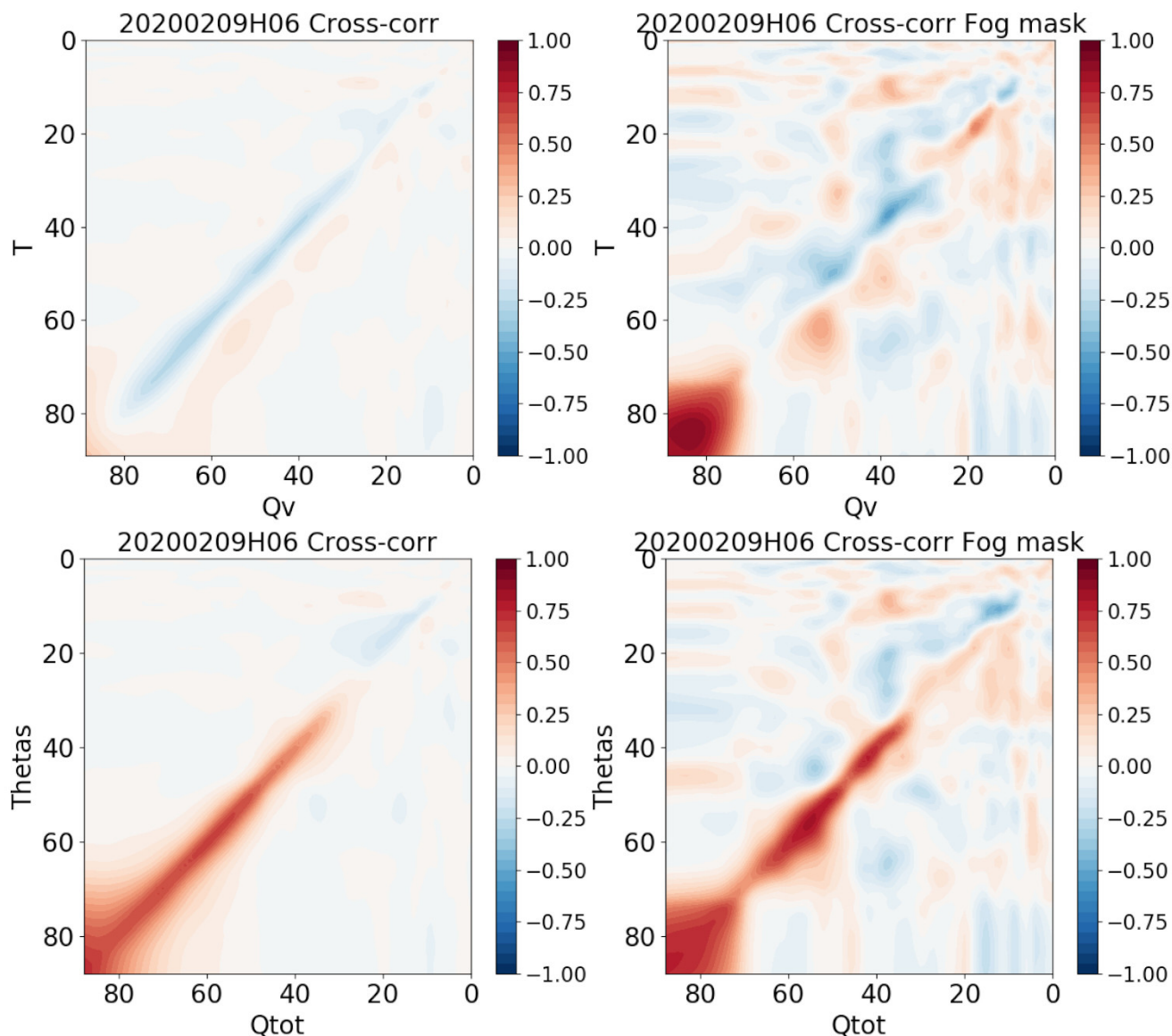
Figure 3. Background error cross-correlation matrices at 06 UTC 9 February 2020 with (right) and without (left) fog mask. Top: between the classical variables (T, q_v) denoted in the axes by "T" and "Qv", respectively. Bottom: between the new conservative variables $((\theta_s)_a, q_t)$ denoted in the axes by "Thetas" and "Qtot", respectively. The axes correspond to the levels of the AROME vertical grid (1 at the top and 90 at the bottom).

background values being much smaller than for the other channels. During the second half of the day, characterized by the presence of clouds around 800 hPa (see Figs. 2 (e) and (f)), the residual values are largely reduced in the frequency bands sensitive to liquid water for channels 5, 6 and 7, especially for EXP as shown by the comparison of the pixels in the dashed
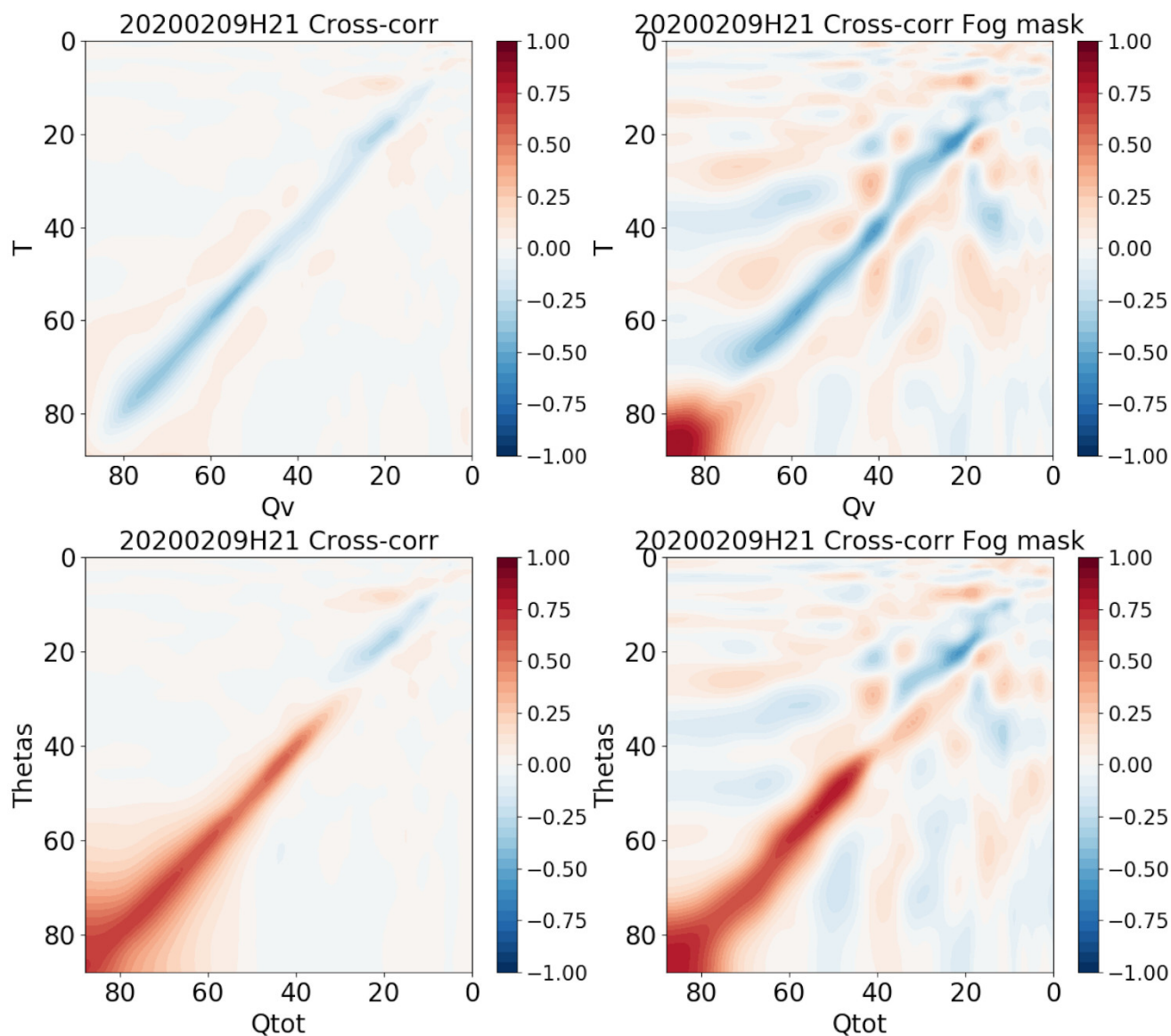
Figure 4. Same as Fig. 3, but at 21 UTC.

rectangular boxes in Figs. 5 (b) and (c). Residuals are also slightly reduced for EXP in the morning and during the fog and low temperature period for the first five channels between 2 and 8 UTC.

In order to quantify these results on 9 February 2020 dataset (all hours and all channels), the bias and root mean square (RMS) error values are computed for the background and the analyses produced by REF and EXP. The innovations are characterized by a RMS error of 3.20 K and a bias of 1.32 K. Both assimilation experiments reduce these two quantities by
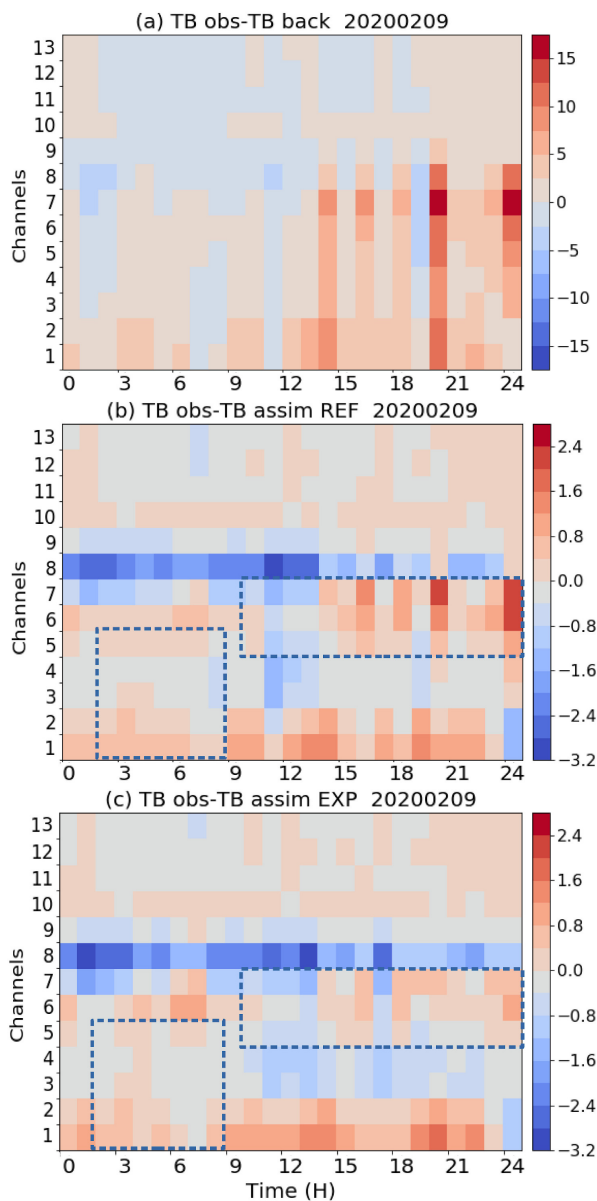
Figure 5. Differences in observed (channels 0 to 5 being located between 22 and 31 GHz and channels 6 to 12 being located between 51 and 58 GHz, HATPRO radiometer) and simulated (with RTTOV-gb) brightness temperatures: (a) from AROME background profiles; (b) from 1D-Var analyses from the REF configuration; and (c) from 1D-Var analyses from the EXP configuration for all hours of the day on 9 February 2020 at Saint-Symphorien (Les Landes region).

265   modifying model profiles. The RMS errors are 0.71 K for EXP and 0.72 K for REF and the biases are -0.17 K for EXP and -0.11 K for REF.

4.3 Vertical profiles of analysis increments
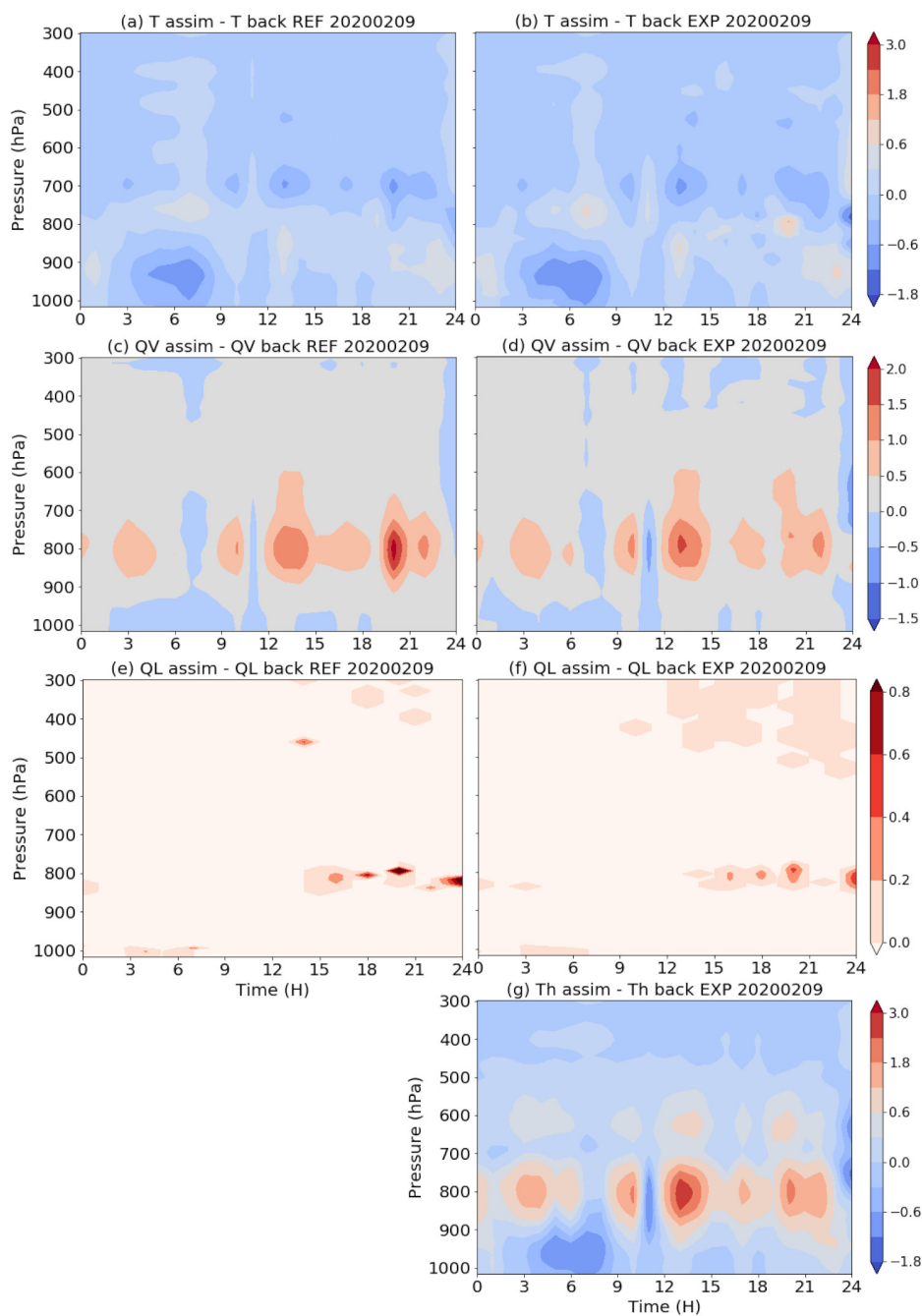
Figure 6. Profiles of analysis increments resulting from two 1D-Var experiments: REF (left) and EXP (right), for: (a)-(b) T in K; (c)-(d) q_v in kg/kg; (e)-(f) q_l in g/kg and (g) $(\theta_s)_a$ in K.

After examining the fit of the two experiments to the observed TBs, we assess the corrections made in model space. Figure 6 shows the increments of (a), (b) temperature, (c), (d) specific humidity, and (e), (f) liquid water for the two experiments REF (left panels) and EXP (right panels). In addition, the increments of $(\theta_s)_a$ are shown in (g).

The temperature increments are mostly located in the lower troposphere (below 650 hPa) with a dominance of negative values of small amplitude (around 0.5 K). This is consistent with negative innovations observed on temperature channels highlighting a warm bias in the background profiles. The areas of maximum cooling take place in cloud layers (inside the thick fog layer below 900 hPa until 9 UTC and around 700 hPa after 12 UTC). The increments are rather similar between REF and EXP, but the positive increments appear to be larger with EXP (e.g. at 08 and 20 UTC around 800 hPa).

Concerning the profiles associated with moist variables, the structures show similarity between the two experiments but with differences in intensity. During the night and in the morning, the q_v increments near the surface are negative. These negative increments are projected into increments having the same sign as T by the strong positive cross-correlations of the $\mathbf{B}_{fog}$ matrix up to 900 hPa (Fig. 3). Thus, the largest negative temperature and specific humidity increments remain confined in the lowest layers.

Liquid water is added in both experiments between 03 UTC and 07 UTC, close to the surface, where the Jacobians of the most sensitive channels to q_l are the largest (not shown). After 14 UTC, values of q_v between 850 and 700 hPa and q_l around 800 hPa are enhanced in both cases, with larger increments for the REF case, in particular at 20 UTC and around midnight. Most of the liquid water is created in low clouds, while for EXP, increments of q_l aloft are more extended in time and in the vertical. For example, at 21 UTC in the REF experiment, the creation of liquid water reaching 0.3 g/kg is observed around 400 hPa. For EXP after 12 UTC, condensation occurs over a thicker atmospheric layer between 500 and 300 hPa. In this experimental set-up, condensed water can be created or removed over the whole column by means of the supersaturation diagnosed at each iteration of the minimisation process (since RTTOV-gb needs (T, q_v, q_l) profiles for the TB computation.) This is a clear advantage over REF which keeps unchanged the vertical structure of the q_l profile from the background. Liquid water is added where it already existed in the background because once the LWP variable is updated, the analyzed q_l profile is just modified proportionally to the ratio between the LWP of the analysis and of the background, as explained in more details by Deblonde and English (2003).

The profiles of increments for $(\theta_s)_a$ show similar structures to the increments of q_v around 800 hPa and to the increments of T below, where temperature Jacobians are the largest (not shown).

5 Conclusions

The aim of this study was to examine the interest of using moist-air entropy potential temperature $(\theta_s)_a$ and total water content q_t to study fog initiation and dissipation at small scale. A 1D-Var system has been used for assimilating brightness temperature (TB) observations from the ground-based HATPRO microwave radiometer installed at Saint-Symphorien (Les Landes region over South-Western France) during the SOFOG3D measurement campaign (winter 2019-2020).

300   The motivations for using the entropy of moist air in atmospheric science by taking into account the absolute value for dry air and water vapour were described by Richardson (1922) and formalized by Hauf and Höller (1987), with the moist-air potential temperature variables θ_s and $(\theta_s)_1$ defined by Marquet (2011). The conservative aspects of these variables and their meteorological properties (fronts, convection, cyclones) have been studied in Marquet (2011), Blot (2013) and Marquet and Geleyn (2015). The links with the definition of the Brunt-Väisälä frequency and the potential vorticity are described in

305 Marquet and Geleyn (2013) and Marquet (2014), while the interest of the absolute entropy to describe the thermodynamics of cyclones is shown in Marquet (2017) and Marquet and Dauhut (2018). The use of the θ_s variable in data assimilation can thus be considered as an additional and natural step that continues these series of studies.

    The 1D-Var system has been adapted to consider these new quantities as control variables. Since the radiative transfer model needs profiles of temperature, water vapour and cloud liquid water for the simulation of TB, an adjustment process has

310 been defined to obtain these quantities from $(\theta_s)_a$ and q_t. The adjoint version of this conversion has been developed for an efficient estimation of the gradient of the cost-function. Dedicated background error covariance matrices have been estimated from the Ensemble Data Assimilation system of AROME. We firstly demonstrated that the matrices for the new variables are less dependent on the meteorological situation (all-weather conditions vs. fog conditions) and on the time of the day (stable conditions by night vs. unstable conditions during the day) leading to potentially more robust estimates. This is an important

315 result as the optimal estimation of the analysis depends on the good specification of the background error covariance matrix which is known to highly vary with weather conditions when using classical control variables.

    The comparison of the new 1D-Var system with a classical system using temperature, water vapour and liquid water path shows rather similar results in terms of fit to observed TB. On the other hand, atmospheric increments on water vapour and liquid water can be locally very different between the two systems.

320   The encouraging results obtained from this feasibility study need to be consolidated by complementary studies. The re-trieved profiles from the 1D-Var should be compared against independent observations (e.g. radiosoundings available from the SOFOG3D field campaign). Observed brightness temperatures at lower elevation angles should be included in the 1D-Var for a better constraint on temperature profiles within the atmospheric boundary layer. Indeed, larger differences in the temperature increment might be obtained between the classical 1D-Var system and the 1D-Var system using the new conservative variables

325 when additional elevation angles are included in the observation vector. Other case studies from the field campaign could also be examined to confirm our first conclusions. Finally, the conversion operator could be improved by accounting not only for liquid water content q_l but also for ice water content q_i (e.g. using a temperature threshold criteria). Indeed, the variable $(\theta_s)_a$ can easily be generalized to the case of the ice phase and mixed phases by taking advantage of the general definition of θ_s and $(\theta_s)_1$, where $L_{vap}\,q_l$ is simply replaced by $L_{vap}\,q_l + L_{sub}\,q_i$.

330   *Code and data availability.* The numerical code of the radiative transfer model RTTOV-gb together with the associated resources (coefficient files) can be downloaded from http://cetemps.aquila.infn.it/rttovgb/rttovgb.html and from https://nwp-saf.eumetsat.int/site/software/rttov-gb/. The 1D-Var software has been adapted from the NWP SAF 1D-Var provided here: https://nwp-saf.eumetsat.int/site/software/

1d-var/ and is available on request to pauline.martinet@meteo.fr. The instrumental data are available on the AERIS website dedicated to the SOFOG3D field experiment: https://sofog3d.aeris-data.fr/catalogue/. AROME backgrounds are available on request to pauline.martinet@meteo.fr.

335 Quicklooks from the cloud radar BASTA are available on: http://basta.projet.latmos.ipsl.fr. The BUMP library to compute background error matrices, developed in the framework of the JEDI project led by the JCSDA (Joint Center for Satellite Data Assimilation, Boulder, Colorado), can be downloaded at https://github.com/JCSDA/saber.

Author contributions. PMarq supervised the work of AB, contributed to the implementation of the new conservative variables in the computation of new background error covariance matrices, participated to the scientific analysis and manuscript redaction. JFM developed the

340 conversion operator and adjoint version, participated in the scientific analysis and manuscript redaction. PMart supervised the modification of the 1D-Var algorithm, supported the use of the EDA to compute background error covariance matrices, provided the instrumental data used in the 1D-Var and participated in the manuscript revision. AB adapted the 1D-Var algorithm and processed all the data, prepared the figures and participated in the manuscript revision. BM developed and adapted the BUMP library to compute the background error covariance matrices for the 1D-Var, and participated in the manuscript revision.

345 *Competing interests.* The authors declare that they have no conflict of interest.

Acknowledgements. The instrumental data used in this study are part of the SOFOG3D experiment. The SOFOG3D field campaign was supported by METEO-FRANCE and ANR through grant AAPG 2018-CE01-0004. Data are managed by the French national center for Atmospheric data and services AERIS. The MWR network deployment was carried out thanks to support by IfU GmbH, the Köln University, the Met-Office, Laboratoire d'Aérologie, Meteoswiss, ONERA, and Radiometer Physics GmbH. MWR data have been made available, qual-

350 ity controlled and processed in the frame of CPEX-LAB (Cloud and Precipitation Exploration LABoratory, www.cpex-lab.de), a competence center within the Geoverbund ABC/J by acting support of Ulrich Löhnert, Rainer Haseneder-Lind and Arthur Kremer from the University of Cologne. This collaboration is driven by the European COST actions ES1303 TOPROF and CA18235 PROBE. Julien Delanoë and Susana Jorquera are thanked for providing the cloud radar quicklooks used in this study for better understanding the meteorological situation. Thibaut Montmerle and Yann Michel are thanked for their support on the use of the AROME EDA to compute background error covariance

355 matrices. The work of Benjamin Ménétrier is funded by the JCSDA (Joint Center for Satellite Data Assimilation, Boulder, Colorado) UCAR SUBAWD2285.

References

Bauer, L. A.: The relation between "potential temperature" and "entropy", Phys. Rev. (Series I), 26, 177–183, https://doi.org/10.1103/PhysRevSeriesI.26.177, 1908.

360   Benjamin, S. G., Brewster, K. A., Brümmer, R., Jewett, B. F., Schlatter, T. W., Smith, T. L., and Stamus, P. A.: An Isentropic Three-Hourly Data Assimilation System Using ACARS Aircraft Observations, Mon. Wea. Rev., 119, 888–906, https://doi.org/10.1175/1520-0493(1991)119<0888:AITHDA>2.0.CO;2, 1991.

Benjamin, S. G., Grell, G. A., Brown, J. M., Smirnova, T. G., and Bleck, R.: Mesoscale Weather Prediction with the RUC Hybrid Isentropic-Terrain-Following Coordinate Model, Mon. Wea. Rev., 132, 473–494, https://doi.org/10.1175/1520-0493(2004)132<0473:MWPWTR>2.0.CO;2, 2004.

365   Betts, A. K.: Non-precipitating cumulus convection and its parameterization, Quart. J. Roy. Meteor. Soc., 99, 178–196, https://doi.org/10.1002/qj.49709941915, 1973.

Blot, E.: Etude de l'entropie humide dans un contexte d'analyse et de prévision du temps, Rapport de stage d'approfondissement EIENM3, Ecole Nationale de la Météorologie. Toulouse, 2013.

370   Brousseau, P., Seity, Y., Ricard, D., and Léger, J.: Improvement of the forecast of convective activity from the AROME-France system, Quart. J. Roy. Meteorol. Soc., 142, 2231–2243, https://doi.org/https://doi.org/10.1002/qj.2822, 2016.

Cimini, D., Hocking, J., De Angelis, F., Cersosimo, A., Di Paola, F., Gallucci, D., Gentile, S., Geraldi, E., Larosa, S., Nilo, S., Romano, F., Ricciardelli, E., Ripepi, E., Viggiano, M., Luini, L., Riva, C., Marzano, F. S., Martinet, P., Song, Y. Y., Ahn, M. H., and Rosenkranz, P. W.: RTTOV-gb v1.0 – updates on sensors, absorption models, uncertainty, and availability, Geosci. Model Dev., 12, 1833–1845,

375   https://doi.org/10.5194/gmd-12-1833-2019, 2019.

Clough, S. A. and Testud, J.: The Fronts-87 experiment and mesoscale frontal dynamics project, WMO Bulletin, 37, 276–281, 1988.

Cullen, M. J. P.: Four-dimensional variational data assimilation: A new formulation of the background-error covariance matrix based on a potential-vorticity representation, Quart. J. Roy. Meteor. Soc., 129, 2777–2796, https://doi.org/https://doi.org/10.1256/qj.02.10, 2003.

De Angelis, F., Cimini, D., Hocking, J., Martinet, P., and Kneifel, S.: RTTOV-gb – adapting the fast radiative transfer model RTTOV for

380   the assimilation of ground-based microwave radiometer observations, Geosci. Model Dev., 9, 2721–2739, https://doi.org/10.5194/gmd-9-2721-2016, 2016.

Deblonde, G. and English, S.: One-Dimensional Variational Retrievals from SSMIS-Simulated Observations, J. Appl. Meteor. Climatol., 42, 1406–1420, https://doi.org/10.1175/1520-0450(2003)042<1406:OVRFSO>2.0.CO;2, 2003.

Delanoë, J., Protat, A., Vinson, J.-P., Brett, W., Caudoux, C., Bertrand, F., du Chatelet, J. P., Hallali, R., Barthes, L., Haeffelin, M., and

385   Dupont, J.-C.: BASTA: A 95-GHz FMCW Doppler Radar for Cloud and Fog Studies, Journal of Atmospheric and Oceanic Technology, 33, 1023–1038, https://doi.org/10.1175/JTECH-D-15-0104.1, 2016.

Desroziers, G.: A Coordinate Change for Data Assimilation in Spherical Geometry of Frontal Structures, Mon. Wea. Rev., 125, 3030–3038, https://doi.org/10.1175/1520-0493(1997)125<3030:ACCFDA>2.0.CO;2, 1997.

Desroziers, G. and Lafore, J.-P.: A Coordinate Transformation for Objective Frontal Analysis, Mon. Wea. Rev., 121, 1531–1553,

390   https://doi.org/10.1175/1520-0493(1993)121<1531:ACTFOF>2.0.CO;2, 1993.

Destouches, M., Montmerle, T., Michel, Y., and Ménétrier, B.: Estimating optimal localization for sampled background-error covariances of hydrometeor variables, Quart. J. Roy. Meteorol. Soc., 147, 74–93, https://doi.org/https://doi.org/10.1002/qj.3906, 2021.

Gustafsson, N., Janjić, T., Schraff, C., Leuenberger, D., Weissmann, M., Reich, H., Brousseau, P., Montmerle, T., Wattrelot, E., Bučánek, A., Mile, M., Hamdi, R., Lindskog, M., Barkmeijer, J., Dahlbom, M., Macpherson, B., Ballard, S., Inverarity, G., Carley, J., Alexander,

395   C., Dowell, D., Liu, S., Ikuta, Y., and Fujita, T.: Survey of data assimilation methods for convective-scale numerical weather prediction at operational centres, Quart. J. Roy. Meteorol. Soc., 144, 1218–1256, https://doi.org/https://doi.org/10.1002/qj.3179, 2018.

Hauf, T. and Höller, H.: Entropy and potential temperature, J. Atmos. Sci., 44, 2887–2901, https://doi.org/10.1175/1520-0469(1987)044<2887:EAPT>2.0.CO;2, 1987.

Marquet, P.: Definition of a moist entropy potential temperature: application to FIRE-I data flights, Quart. J. Roy. Meteorol. Soc., 137,

400   768–791, https://doi.org/10.1002/qj.787, 2011.

Marquet, P.: On the definition of a moist-air potential vorticity., Quart. J. Roy. Meteorol. Soc., 140, 917–929, https://doi.org/10.1002/qj.2182, 2014.

Marquet, P.: A Third-Law Isentropic Analysis of a Simulated Hurricane, J. Atmos. Sci., 74, 3451–3471, https://doi.org/10.1175/JAS-D-17-0126.1, 2017.

405 Marquet, P. and Bechtold, P.: A new Estimated Inversion Strength (EIS) based on the moist-air entropy, Research activities in Earth system modelling. Working Group on Numerical Experimentation. Report No. 50. WCRP (Blue Book) Report No.12/2020. Ed. E. Astakhova, WMO, Geneva, 50, 1–2, http://bluebook.meteoinfo.ru/uploads/2020/docs/04_Marquet_Pascal_NewEntropyEIS.pdf, 2020.

Marquet, P. and Dauhut, T.: Reply to "Comments on 'A third-law isentropic analysis of a simulated hurricane'", J. Atmos. Sci., 75, 3735–3747, https://doi.org/10.1175/JAS-D-18-0126.1, 2018.

410 Marquet, P. and Geleyn, J.-F.: On a general definition of the squared Brunt-Väisälä frequency associated with the specific moist entropy potential temperature, Quart. J. Roy. Meteorol. Soc., 139, 85–100, https://doi.org/10.1002/qj.1957, 2013.

Marquet, P. and Geleyn, J.-F.: Formulations of moist thermodynamics for atmospheric modelling, in: Parameterization of Atmospheric Convection. Vol II: Current Issues and New Theories, edited by Plant, R. S. and Yano, J.-I., *World Scientific*, pp. 221–274, Imperial College Press, https://doi.org/10.1142/9781783266913_0026, 2015.

415 Martinet, P., Cimini, D., Burnet, F., Ménétrier, B., Michel, Y., and Unger, V.: Improvement of numerical weather prediction model analysis during fog conditions through the assimilation of ground-based microwave radiometer observations: a 1D-Var study, Atmos. Meas. Tech., 13, 6593–6611, https://doi.org/10.5194/amt-13-6593-2020, 2020.

Ménétrier, B. and Montmerle, T.: Heterogeneous background-error covariances for the analysis and forecast of fog events, Quart. J. Roy. Meteor. Soc., 137, 2004–2013, https://doi.org/10.1002/qj.802, 2011.

420 Michel, Y., Auligné, T., and Montmerle, T.: Heterogeneous Convective-Scale Background Error Covariances with the Inclusion of Hydrometeor Variables, Mon. Wea. Rev., 139, 2994–3015, https://doi.org/10.1175/2011MWR3632.1, 2011.

Montmerle, T. and Berre, L.: Diagnosis and formulation of heterogeneous background-error covariances at the mesoscale, Quart. J. Roy. Meteor. Soc., 136, 1408–1420, https://doi.org/10.1002/qj.655, 2010.

Richardson, L. F.: Weather prediction by numerical process, pp. 1–229, Cambridge University Press, 1922.

425 Rodgers, C. D.: Retrieval of atmospheric temperature and composition from remote measurements of thermal radiation, Rev. Geophys., 14, 609–624, https://doi.org/10.1029/RG014i004p00609, 1976.

Rose, T., Crewell, S., Löhnert, U., and Simmer, C.: A network suitable microwave radiometer for operational monitoring of the cloudy atmosphere, Atmos. Res., 75, 183–200, https://doi.org/10.1016/j.atmosres.2004.12.005, 2005.

Seity, Y., Brousseau, P., Malardel, S., Hello, G., Bénard, P., Bouttier, F., Lac, C., and Masson, V.: The AROME-France convective-scale

430   operational model, Mon. Wea. Rev., 139, 976–991, https://doi.org/10.1175/2010MWR3425.1, 2011.

Shapiro, M. A. and Hastings, J. T.: Objective cross-section analyses by Hermite polynomial interpolation on isentropic surfaces, J. Appl. Meteorol. Climatol., 12, 753–762, https://doi.org/10.1175/1520-0450(1973)012<0753:OCSABH>2.0.CO;2, 1973.

Wlasak, M., Nichols, N. K., and Roulstone, I.: Use of potential vorticity for incremental data assimilation, Quart. J. Roy. Meteor. Soc., 132, 2867–2886, https://doi.org/https://doi.org/10.1256/qj.06.02, 2006.